# Possible new chiral system with two high-$j$ valence protons

L. Mu (穆琳),[1,2] H. Jia (贾慧),[3,*] B. Qi (亓斌),[4] and J. G. Deng (邓军刚)[1,2,†]

[1]*College of Mathematics and Physics, China Three Gorges University, Yichang 443002, China*

[2]*Center for Astronomy and Space Sciences, China Three Gorges University, Yichang 443002, China*

[3]*School of Science, Harbin Institute of Technology, Weihai 264209, China*

[4]*Shandong Provincial Key Laboratory of Nuclear Science, Nuclear Energy Technology and Comprehensive Utilization, Weihai Frontier Innovation Institute of Nuclear Technology, School of Nuclear Science, Energy and Power Engineering, Shandong University, Shandong 250061, China*

(Received 8 December 2024; revised 19 March 2025; accepted 7 May 2025; published 28 May 2025)

The chirality in Xe isotopes is investigated by using the constrained triaxial covariant density functional theory (CDFT) and quantum particle rotor model (PRM) calculations. The CDFT results show that the $\pi g_{9/2}^{-1} \otimes \pi h_{11/2}^{1}$ configurations with high-$j$ particle-hole character exhibit significant triaxial deformations in $^{116,118,120,122,124,126}$Xe, making them suitable for establishing chirality. In $^{118}$Xe and $^{120}$Xe, the available experimental energy spectra and the electromagnetic transition probabilities with the $\pi g_{9/2}^{-1} \otimes \pi h_{11/2}^{1}$ configuration are described well by PRM calculations. A systematic comparison with the chiral doublet bands based on the $\pi g_{9/2}^{-1} \otimes \nu h_{11/2}^{1}$ configuration is also discussed. The present work proposes a new chiral system formed by the coupling of two high-$j$ valence protons, contributing to the exploration of the key scientific question regarding the universality of nuclear chirality.

DOI: 10.1103/PhysRevC.111.054321

## I. INTRODUCTION

Chirality is a subject of general interest in physics, chemistry, and biology. In nuclear physics, chiral symmetry was predicted by Frauendorf and Meng [1]. They pointed out that, in the intrinsic frame of a rotating triaxial nucleus with a few high-$j$ valence particles and a few high-$j$ valence holes, the total angular momentum vector may lie outside the three principal planes, referred to as chiral geometry [1]. Due to the chiral symmetry breaking, a pair of nearly degenerate $\Delta I = 1$ bands with the same parity, i.e., chiral doublet bands, are expected to be observed in the laboratory frame [1]. In 2001, chiral doublet bands based on the $\pi h_{11/2}^{1} \otimes \nu h_{11/2}^{-1}$ configuration were observed for the first time in the $A \approx 130$ mass region [2]. A key scientific question then arises: "to what extent is nuclear chirality universal?" [3]. To investigate this, researchers have made extensive experimental efforts to search for chiral doublet bands across the nuclear chart. So far, more than 50 candidate chiral nuclei have been reported in the $A \approx 80$, 100, 130, and 190 mass regions [3–11], including numerous odd-odd and odd-$A$ nuclei, as well as several even-even nuclei. It should be noted that nearly all reported chiral configurations are formed by the coupling of valence proton(s) and neutron(s). In comparison, only four candidate chiral doublets based on the same kind of fermion coupling [i.e., $\nu h_{11/2}^{1} \otimes \nu(g_{7/2}, d_{5/2})^{-1}$] have been reported. in $^{104}$Mo [12], $^{106}$Mo [13], $^{110}$Ru [14], and $^{112}$Ru [14]. However, due to the configuration involving low-$j$ pseudospin doublet states $g_{7/2}$ and $d_{5/2}$, an alternative interpretation of pseudospin doublet bands cannot be ruled out. Thus, to establish the more general nature of chirality, it is of high scientific interest to explore whether the same kind of fermion coupling, such as valence proton-proton coupling or valence neutron-neutron coupling, can form chiral systems. Meanwhile, these systems should exclude the interference from pseudospin symmetry.

For the specific configurations we expect, the excitation of nucleons across the closed shell is an effective pathway to obtain them. This excitation allows valence protons (or valence neutrons) to simultaneously occupy high-$j$ particle and hole orbitals, thereby satisfying one of the key conditions for the formation of chirality. Guided by this, we have noted the presence of rotational bands based on the $\pi g_{9/2}^{-1} \otimes \pi h_{11/2}^{1}$ configuration in $^{118,120}$Xe ($Z = 54$) near the $Z = 50$ closed shell [15,16]. This configuration involves a holelike $g_{9/2}$ quasiproton and a particlelike $h_{11/2}$ quasiproton, favoring the formation of chirality while simultaneously avoiding interference from pseudospin symmetry. Thus, the $\pi g_{9/2}^{-1} \otimes \pi h_{11/2}^{1}$ configuration in even-even Xe isotopes serves as a good research object for investigating whether the same type of fermion coupling can also give rise to chirality. In fact, there is a competition between breakings of a proton pair and a neutron pair in even-even Xe nuclei, which leads to various configurations in this region. Among these, the two-neutron configuration $\nu h_{11/2} \otimes \nu(g_{7/2}, d_{5/2})$ has also been identified [15,17,18]. However, as mentioned above, this configuration involves low-$j$ pseudospin orbitals and is thus not included in this work.

Another interesting point is that, although chirality has been widely reported in odd-odd and odd-$A$ nuclei, its study in even-even nuclei is still relatively limited. So far, only

*Contact author: jiahui@sdu.edu.cn

†Contact author: dengjungang@ctgu.edu.cn

 ©2025 American Physical Society

six even-even nuclei have been reported to exhibit chirality, including the aforementioned $^{104,106}$Mo [12,13], $^{110,112}$Ru [14], as well as $^{136,138}$Nd [19,20]. Notably, in $^{136}$Nd, five pairs of chiral doublet bands with four-quasiparticle (4qp) and six-quasiparticle (6qp) configurations have been identified, representing the largest set of nearly degenerate bands reported in a single nucleus to date [19]. In this work, the investigation of the $\pi g_{9/2}^{-1} \otimes \pi h_{11/2}^{1}$ configuration in Xe isotopes could also help in exploring promising candidates for chiral nuclei in an even-even system.

It is well known that, in addition to the proper particle-hole configuration, triaxial deformation is the other necessary condition for nuclear chirality. Therefore, to explore the chirality of the $\pi g_{9/2}^{-1} \otimes \pi h_{11/2}^{1}$ configuration in even-even Xe isotopes, a reliable theoretical approach capable of obtaining configurations and corresponding deformations in nuclei is essential. The adiabatic and configuration fixed constrained triaxial covariant density functional theory (CDFT) is a successful method for this purpose, having been widely employed to predict and describe the existence of nuclear chirality or multiple chirality [21–32]. In the present work, we adopt the constrained CDFT to systematically study the deformations and corresponding configurations in even-even Xe isotopes (viz., $^{116,118,120,122,124,126}$Xe), aiming to explore whether the $\pi g_{9/2}^{-1} \otimes \pi h_{11/2}^{1}$ configuration, characterized by valence proton-proton coupling, can form a chiral system. Subsequently, we examine the manifestation of chirality for the $\pi g_{9/2}^{-1} \otimes \pi h_{11/2}^{1}$ bands in $^{118}$Xe and $^{120}$Xe using the quantum particle rotor model (PRM), which has proved to be a reliable tool for studying the properties of chiral doublet bands [32–38].

## II. THEORETICAL FRAMEWORK

### A. Covariant density functional theory

The detailed formalism and numerical techniques of the adiabatic and configuration fixed constrained CDFT calculation adopted in this work can be found in Refs. [21,22,39] and references therein. Here "adiabatic" means that the nucleons always occupy the lowest single-particle levels during the constraint process, while "configuration fixed" means that the nucleons must occupy the same combination of the single-particle levels during the constraint process. Only a brief introduction is presented below.

The CDFT starts from a standard effective Lagrangian density constructed with the degrees of freedom associated with the nucleon field ($\psi$), two isoscalar meson fields ($\sigma$ and $\omega_\mu$), the isovector meson field ($\boldsymbol{\rho}_\mu$), and the photon field ($A_\mu$). Under "mean-field" and "no-sea" approximations, one can derive the corresponding energy density functional, from which one finds immediately the equation of motion for a single-nucleon orbit $\psi_i(\boldsymbol{r})$ with the help of the variational principle,

$$\{\alpha \cdot [\boldsymbol{p} - \boldsymbol{V}(\boldsymbol{r})] + \beta m^*(\boldsymbol{r}) + V_0(\boldsymbol{r})\}\psi_i(\boldsymbol{r}) = \epsilon_i \psi_i(\boldsymbol{r}), \tag{1}$$

where $m^*(\boldsymbol{r})$ is defined as $m^*(\boldsymbol{r}) \equiv m + g_\sigma \sigma(\boldsymbol{r})$, with $m$ referring to the mass of the bare nucleon. The repulsive vector potential $V_0(\boldsymbol{r})$ is the timelike component of vector potential, and the time-odd fields $\boldsymbol{V}(\boldsymbol{r})$ are the spacelike components of vector fields. More details about the solution of the Dirac equation (1) can be found in Refs. [40,41].

### B. Quantum particle rotor model

The PRM is a quantum mechanical method that describes the system in the laboratory framework and yields directly the energy splitting and tunneling probabilities between doublet bands. It has been extensively used in the investigation of chiral doublet bands [32–36]. A detailed description of the model can be found in Refs. [1,37,38,42,43]. Here, we provide a brief description.

The PRM Hamiltonian of the proton-proton coupling system can be expressed as

$$\hat{H} = \hat{H}_{\text{core}} + \hat{H}_p + \hat{H}_{p'}, \tag{2}$$

where $p$ and $p'$ refer to the valence protons outside the core. The Hamiltonian of the core is

$$\hat{H}_{\text{core}} = \sum_{i=1}^{3} \frac{\hat{R}_i^2}{2\mathcal{J}_i} = \sum_{i=1}^{3} \frac{(\hat{I}_i - \hat{j}_{pi} - \hat{j}_{p'i})^2}{2\mathcal{J}_i}, \tag{3}$$

with the index $i = 1, 2, 3$ denoting the three principal axes in the body-fixed frame. Here $\hat{R}_i$ and $\hat{I}_i$ are the angular momentum operators of the core and the total nucleus, while $\hat{j}_{p(p')i}$ is the angular momentum operator of the valence proton. Moreover, $\mathcal{J}_i$ respresents the moment of inertia for irrotational flow, i.e., $\mathcal{J}_i = \mathcal{J}_0 \sin^2(\gamma - 2\pi i/3)$.

The Hamiltonian $\hat{H}_{p(p')}$ describes a single proton outside of the rotor. For a single-$j$ model, $\hat{H}_{p(p')}$ can be given as

$$\hat{H}_{p(p')} = \pm\frac{1}{2}C\left\{\cos\gamma\left[\hat{j}_3^2 - \frac{j(j+1)}{3}\right] + \frac{\sin\gamma}{2\sqrt{3}}(\hat{j}_+^2 + \hat{j}_-^2)\right\}, \tag{4}$$

where the plus sign refers to a particle and the minus sign to a hole, and the coupling parameter $C$ is proportional to the quadrupole deformation parameter $\beta$ of the rotor.

## III. RESULTS AND DISCUSSION

First, we will carry out the adiabatic and configuration fixed constrained triaxial CDFT calculations to obtain the single-particle energy levels, deformation parameters $(\beta, \gamma)$, as well as the potential energy curves (PECs) for $^{116-126}$Xe isotopes, which will be used to analyze the possible configurations and deformations to search for the existence of chirality. Second, adopting the deformation parameters obtained from CDFT, we will calculate the energy spectra and electromagnetic properties for the $\pi g_{9/2}^{-1} \otimes \pi h_{11/2}^{1}$ configuration in $^{118}$Xe and $^{120}$Xe using the quantum particle rotor model (PRM), and then compare these calculated results with experimental data. Finally, a systematic study of excitation energies, the staggering parameters, and moments of inertia will be performed for the $\pi g_{9/2}^{-1} \otimes \pi h_{11/2}^{1}$ configuration in $^{118}$Xe and $^{120}$Xe, as well as the $\pi g_{9/2}^{-1} \otimes \nu h_{11/2}^{1}$ configuration in $^{98}$Tc, $^{100}$Tc, $^{102}$Rh, $^{104}$Rh, $^{106}$Rh, and $^{104}$Ag.

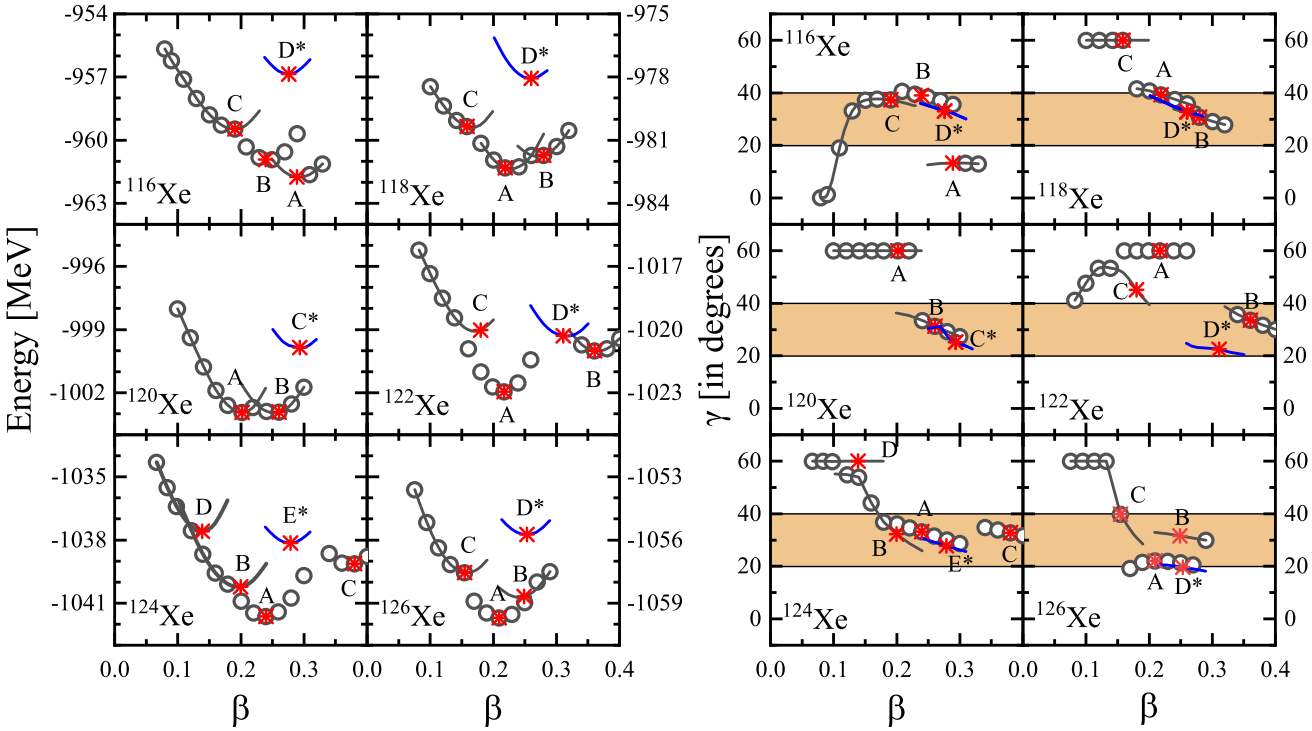


FIG. 1. The energy surfaces (left) and triaxiality parameter $\gamma$ (right) as a function of the deformation parameter $\beta$ in the triaxial CDFT with the PC-PK1 interaction for $^{116,118,120,122,124,126}$Xe. Open circles and solid lines represent the adiabatic and configuration-fixed constrained triaxial CDFT calculations, respectively. The minima in the energy surfaces for the fixed configuration are marked by stars and labeled as A, B, C, D, and E. The states corresponding to the unpaired nucleon configuration $\pi g_{9/2}^{-1} \otimes \pi h_{11/2}^{1}$ are indicated by blue color and asterisks. The shaded area in the right panel represents the values of $\gamma$ favorable for nuclear chirality.

### A. Covariant density functional theory results

In the present calculations, the point-coupling density functional PC-PK1 [44] is adopted. Pairing correlations are neglected for simplicity, though their possible influence on the description of nuclear properties in even-even Xe isotopes remains to be explored in the future. The Dirac equation is solved in a set of three-dimensional harmonic oscillator bases with 12 major oscillator shells.

Figure 1 shows the theoretical results based on adiabatic and configuration-fixed constrained triaxial CDFT. The calculated potential energy curves in $^{116,118,120,122,124,126}$Xe are presented in the left panel of Fig. 1. The local minima in the potential energy curves are marked by stars and labeled by letters of the alphabet. The triaxiality parameter $\gamma$ obtained by minimizing the energy is given as a function of $\beta$ in the right panel of Fig. 1. The shaded regions in the figures represent the values of $\gamma$ that are favorable for nuclear chirality. The excited configurations are represented by blue solid lines, which were obtained by exciting the proton from the $g_{9/2}$ shell to the $h_{11/2}$ shell. The calculated total energies $E_{\rm tot}$, triaxial deformation parameters $\beta$ and $\gamma$, corresponding valence nucleon, and unpaired nucleon configurations of the minima are listed in Table I. The valence proton configurations are drawn from 50 nucleons, and the valence neutron configurations are from 64 nucleons.

As shown in Fig. 1, state A represents the ground state for the Xe isotopes, with the quadrupole deformation parameter $\beta$ being 0.29 in $^{116}$Xe and approximately 0.22 in $^{118-126}$Xe. The triaxial deformation parameter $\gamma$ further reveals the shape evolution of the ground states across the Xe isotopes: the shape transitions from a prolate deformation in $^{116}$Xe to a triaxial form in $^{118}$Xe, then to oblate shapes in $^{120}$Xe and $^{122}$Xe, and finally to triaxial shapes again in $^{124}$Xe and $^{126}$Xe. For the excited states, the state D in $^{116}$Xe ($\beta = 0.28$, $\gamma = 33.0^\circ$), the state D in $^{118}$Xe ($\beta = 0.26$, $\gamma = 32.8^\circ$), the state C in $^{120}$Xe ($\beta = 0.29$, $\gamma = 25.3^\circ$), the state D in $^{122}$Xe ($\beta = 0.31$, $\gamma = 22.5^\circ$), the state E in $^{124}$Xe ($\beta = 0.28$, $\gamma = 27.8^\circ$), and the state D in $^{126}$Xe ($\beta = 0.25$, $\gamma = 19.7^\circ$) correspond to the unpaired nucleon configuration $\pi g_{9/2}^{-1} \otimes \pi h_{11/2}^{1}$. Each of these states exhibits obvious triaxial deformation and high-$j$ particle-hole configuration. Thus, it is expected that chiral doublet bands could be constructed on these excited states in $^{116-126}$Xe.

It is worth noting that a negative parity $\Delta I = 1$ band (labeled as 1 in Refs. [15,16]) with the $\pi g_{9/2}^{-1} \otimes \pi h_{11/2}^{1}$ configuration has already been observed in both $^{118}$Xe and $^{120}$Xe. The $8^-$ state in $^{118}$Xe and $6^-$ state in $^{120}$Xe, corresponding to the bandheads, have excitation energies of 3.051 and 2.729 MeV, respectively. From Table I, one can see that the calculated excitation energies of the $\pi g_{9/2}^{-1} \otimes \pi h_{11/2}^{1}$ configuration for $^{118}$Xe and $^{120}$Xe somewhat overestimate the corresponding data, which might be due to the lack of pairing correlations. Additionally, the $\pi g_{9/2}^{-1} \otimes \pi h_{11/2}^{1}$ bands in $^{118}$Xe and $^{120}$Xe had shown experimental indications of triaxial de-

TABLE I. The total energies $E_{\rm tot}$, triaxial-deformation parameters $\beta$ and $\gamma$, and the the corresponding configurations (both valence nucleon and unpaired nucleon) of minima for states A–E obtained by the adiabatic and configuration-fixed constrained triaxial CDFT calculations for $^{116\text{–}126}$Xe. The configurations of the valence proton are drawn from 50 nucleons, and those of the valence neutron are from 64 nucleons. The $(g_{7/2}, d_{5/2})$ and $(s_{1/2}, d_{3/2})$ orbitals are represented by $(g, d)$ and $(s, d)$, respectively.

| Nuclei | State | Configuration | | $E_{\rm tot}$ | $(\beta, \gamma)$ |
|---|---|---|---|---|---|
| | | Valence nucleons | Unpaired nucleons | (MeV) | (MeV) |
| $^{116}$Xe | A | $\pi(g,d)^4 \otimes \nu(g,d)^{-6}h^4_{11/2}$ | g.s. | −961.75 | (0.29, 13.3°) |
| | B | $\pi(g,d)^4 \otimes \nu(g,d)^{-4}h^2_{11/2}$ | | −960.93 | (0.24, 39.1°) |
| | C | $\pi(g,d)^4 \otimes \nu(g,d)^{-2}$ | | −959.47 | (0.19, 37.3°) |
| | D* | $\pi g^{-1}_{9/2}h^1_{11/2}(g,d)^4 \otimes \nu(g,d)^{-4}h^2_{11/2}$ | $\pi g^{-1}_{9/2}h^1_{11/2}$ | −956.86 | (0.28, 33.0°) |
| $^{118}$Xe | A | $\pi(g,d)^4 \otimes \nu(g,d)^{-2}h^2_{11/2}$ | g.s. | −982.31 | (0.22, 39.3°) |
| | B | $\pi(g,d)^4 \otimes \nu(g,d)^{-4}h^4_{11/2}$ | | −981.71 | (0.28, 30.7°) |
| | C | $\pi(g,d)^4$ | | −980.35 | (0.16, 60.0°) |
| | D* | $\pi g^{-1}_{9/2}h^1_{11/2}(g,d)^4 \otimes \nu(g,d)^{-2}h^2_{11/2}$ | $\pi g^{-1}_{9/2}h^1_{11/2}$ | −978.07 | (0.26, 32.8°) |
| $^{120}$Xe | A | $\pi(g,d)^4 \otimes \nu h^2_{11/2}$ | g.s. | −1002.94 | (0.20, 60.0°) |
| | B | $\pi(g,d)^4 \otimes \nu(g,d)^{-2}h^4_{11/2}$ | | −1002.92 | (0.26, 31.3°) |
| | C* | $\pi g^{-1}_{9/2}h^1_{11/2}(g,d)^4 \otimes \nu(g,d)^{-2}h^4_{11/2}$ | $\pi g^{-1}_{9/2}h^1_{11/2}$ | −999.85 | (0.29, 25.3°) |
| $^{122}$Xe | A | $\pi(g,d)^4 \otimes \nu h^4_{11/2}$ | g.s. | −1022.95 | (0.22, 60.0°) |
| | B | $\pi h^2_{11/2}p^{-2}_{1/2}(g,d)^4 \otimes \nu(g,d)^{-2}h^6_{11/2}$ | | −1021.01 | (0.36, 33.5°) |
| | C | $\pi(g,d)^4 \otimes \nu(s,d)^2h^2_{11/2}$ | | −1020.02 | (0.18, 45.1°) |
| | D* | $\pi g^{-1}_{9/2}h^1_{11/2}(g,d)^4 \otimes \nu(g,d)^{-2}h^6_{11/2}$ | $\pi g^{-1}_{9/2}h^1_{11/2}$ | −1020.29 | (0.31, 22.5°) |
| $^{124}$Xe | A | $\pi(g,d)^4 \otimes \nu h^6_{11/2}$ | g.s. | −1041.63 | (0.24, 33.2°) |
| | B | $\pi(g,d)^4 \otimes \nu(s,d)^2h^4_{11/2}$ | | −1040.22 | (0.20, 32.2°) |
| | C | $\pi h^2_{11/2}p^{-2}_{1/2}(g,d)^4 \otimes \nu(g,d)^{-2}h^8_{11/2}$ | | −1039.13 | (0.38, 32.7°) |
| | D | $\pi(g,d)^4 \otimes \nu(s,d)^4h^2_{11/2}$ | | −1037.59 | (0.14, 60.0°) |
| | E* | $\pi g^{-1}_{9/2}h^1_{11/2}(g,d)^4 \otimes \nu h^6_{11/2}$ | $\pi g^{-1}_{9/2}h^1_{11/2}$ | −1038.14 | (0.28, 27.8°) |
| $^{126}$Xe | A | $\pi(g,d)^4 \otimes \nu(s,d)^2h^6_{11/2}$ | g.s. | −1059.69 | (0.21, 22.1°) |
| | B | $\pi(g,d)^4 \otimes \nu h^8_{11/2}$ | | −1058.67 | (0.25, 31.5°) |
| | C | $\pi(g,d)^4 \otimes \nu(g,d)^{-2}(s,d)^6h^4_{11/2}$ | | −1057.54 | (0.15, 39.9°) |
| | D* | $\pi g^{-1}_{9/2}h^1_{11/2}(g,d)^4 \otimes \nu(g,d)^{-2}(s,d)^4h^6_{11/2}$ | $\pi g^{-1}_{9/2}h^1_{11/2}$ | −1055.75 | (0.25, 19.7°) |

formation. If such a band were axially symmetric, the $K$ value would be 4 or 5, meaning that $\gamma$-ray decays from this band to the ground-state band with $K = 0$ would be strongly inhibited, thereby resulting in the formation of a long-lived $K$ isomer [45]. However, in fact, the experimental observations do not match this assumed scenario. It can be seen from the available data reported in Refs. [15,16] that, for the $\pi g^{-1}_{9/2} \otimes \pi h^1_{11/2}$ bands in $^{118}$Xe and $^{120}$Xe, the absence of the $K$ isomer and the observation of $\gamma$ rays deexcited from these bands to the ground-state band point to the presence of triaxial deformation [46,47]. These findings associated with excitation energies and triaxial deformations are consistent with the current predictions, suggesting the validity of the CDFT calculations.

Given that the $\pi g^{-1}_{9/2} \otimes \pi h^1_{11/2}$ configuration has been identified in $^{118}$Xe and $^{120}$Xe, we present in Fig. 2 the single-particle energy levels of the proton near the Fermi surface for this configuration in both nuclei, as calculated by CDFT, to provide a clearer picture of its formation mechanism. The single-particle energy levels of the ground state are also included in Fig. 2. For the ground state, four paired protons are located at the bottom of the $gd$ shell, just above the $Z = 50$ shell gap. By promoting one proton from the highest level of the $g_{9/2}$ orbitals across the $Z = 50$ shell to the lowest level of the $h_{11/2}$ orbitals, the $\pi g^{-1}_{9/2} \otimes \pi h^1_{11/2}$ valence nucleon configuration shown in Fig. 2 is created. This configuration exhibits a pronounced particle-hole character, together with significant triaxial deformation, making it a good candidate for chirality.

### B. Quantum particle rotor model results

To further examine the hypothesis of the chirality for the $\pi g^{-1}_{9/2} \otimes \pi h^1_{11/2}$ bands in $^{118}$Xe and $^{120}$Xe, we employed PRM to analyze these bands. In our PRM calculations, the quadrupole deformation values obtained from CDFT, i.e., ($\beta = 0.26$, $\gamma = 32.8°$) for $^{118}$Xe and ($\beta = 0.29$, $\gamma = 25.3°$) for $^{120}$Xe, were initially used as input parameters. By adjusting the triaxial deformation parameter $\gamma$ in 2° increments, the theoretical results with $\gamma = 34.8°$ (+2°) for $^{118}$Xe and $\gamma = 21.3°$ (−4°) for $^{120}$Xe demonstrated better consistency with experimental data. A similar treatment can be found in other

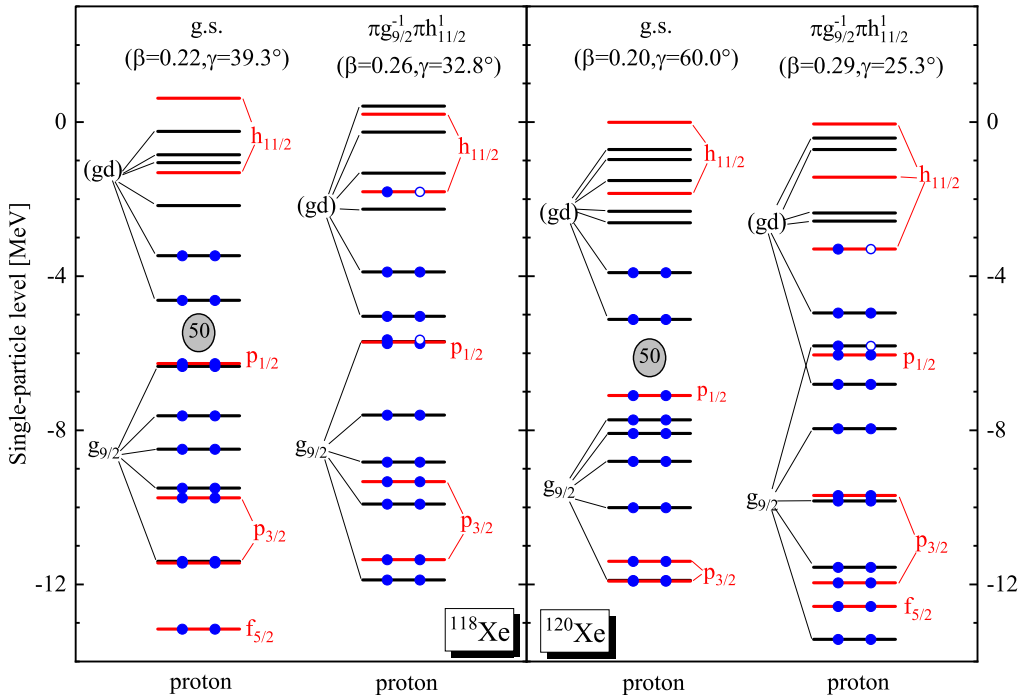


FIG. 2. Single proton levels near the Fermi surface for the ground state and $\pi g_{9/2}^{-1} \otimes \pi h_{11/2}^{1}$ valence nucleon configuration in $^{118}$Xe (left panel) and $^{120}$Xe (right panel).

PRM calculations [8,48,49]. The moments of inertia $\mathcal{J}_0 = 34\,\hbar^2/\text{MeV}$ for both nuclei are adjusted by fitting to the experimental energy spectra. For the electromagnetic transition, the empirical intrinsic quadrupole moment $Q_0 = (3/\sqrt{5\pi})R_0^2 Z\beta$, where $R_0 = 1.2\ \text{fm} \times A^{1/3}$ is the nuclear radius, is taken as 3.68 $e$b for $^{118}$Xe and 4.15 $e$b for $^{120}$Xe. The gyromagnetic ratios of $g_R = Z/A$, $g_\pi(g_{9/2}) = 1.261$ and $g_\pi(h_{11/2}) = 1.214$ are adopted.

The calculated energy spectra $E(I)$ and the reduced transition probability ratios $B(M1)/B(E2)$ for the yrast and yrare bands with the $\pi g_{9/2}^{-1} \otimes \pi h_{11/2}^{1}$ configuration in $^{118}$Xe and $^{120}$Xe are presented in Fig. 3. For comparison, the experimental results obtained from band 1 in $^{118}$Xe [15] and band 1 in $^{120}$Xe [16] are also included in Fig. 3. As shown in Figs. 3(a1) and 3(a2), the experimental energy spectra of $^{118}$Xe and $^{120}$Xe are both excellently reproduced by the PRM calculations. In Figs. 3(b1) and 3(b2), the experimental $B(M1)/B(E2)$ values for bands 1 in $^{118}$Xe and $^{120}$Xe remain approximately constant around 2 $\mu_N^2/e^2\text{b}^2$, with no significant odd-even staggering observed. The calculated $B(M1)/B(E2)$'s demonstrate a generally good agreement with the experimental values for both nuclei, except at $I = 14\hbar$ in $^{118}$Xe and $I = 16\hbar$ in $^{120}$Xe, where kinks appear. These kinks might be due to wave function mixing between the yrast and yrare bands, as discussed in Ref. [50]. Overall, the consistency between the experimental data and PRM results supports the triaxial deformation of the $\pi g_{9/2}^{-1} \otimes \pi h_{11/2}^{1}$ configuration predicted by CDFT, thereby further strengthening the hypothesis of chirality in band 1 of both $^{118}$Xe and $^{120}$Xe. It would be very interesting to search for their chiral partner bands in future experiments.

The rotational motion of triaxial nuclei attains a chiral character if the angular momentum has substantial projections on all three principal axes of the triaxially deformed nucleus [1]. The successful reproduction of the energy spectra and available electromagnetic transition probabilities for bands 1 in $^{118}$Xe and $^{120}$Xe motivates us to investigate their angular momentum geometry. Figure 4 presents the expectation values of the squared angular momentum components of the core $R$, the $g_{9/2}$ valence proton $J_p(g_{9/2})^{-1}$, and the $h_{11/2}$ valence

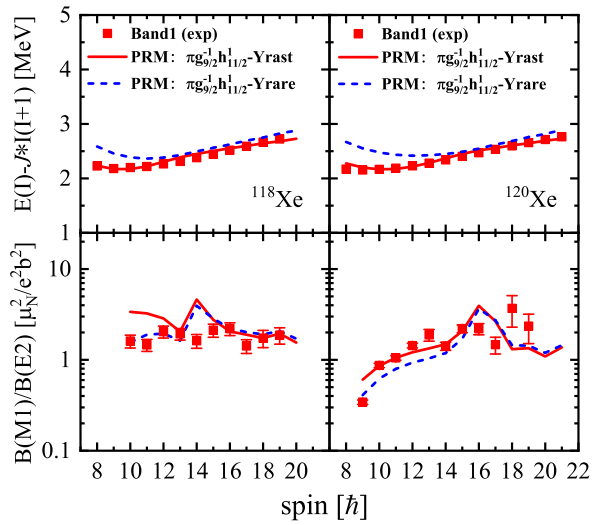


FIG. 3. (a1) and (b1): Experimental excitation energies relative to a rigid-rotor reference and $B(M1)/B(E2)$ ratios for band 1 with the $\pi g_{9/2}^{-1} \otimes \pi h_{11/2}^{1}$ configuration in $^{118}$Xe [15] as a function of spin, in comparison with the PRM calculations. (a2) and (b2): Same as (a1) and (b1) but for $^{120}$Xe [16]. The $J$ parameters are evaluated from the relation $J = 0.007 \times (\frac{158}{A})^{5/3}$.

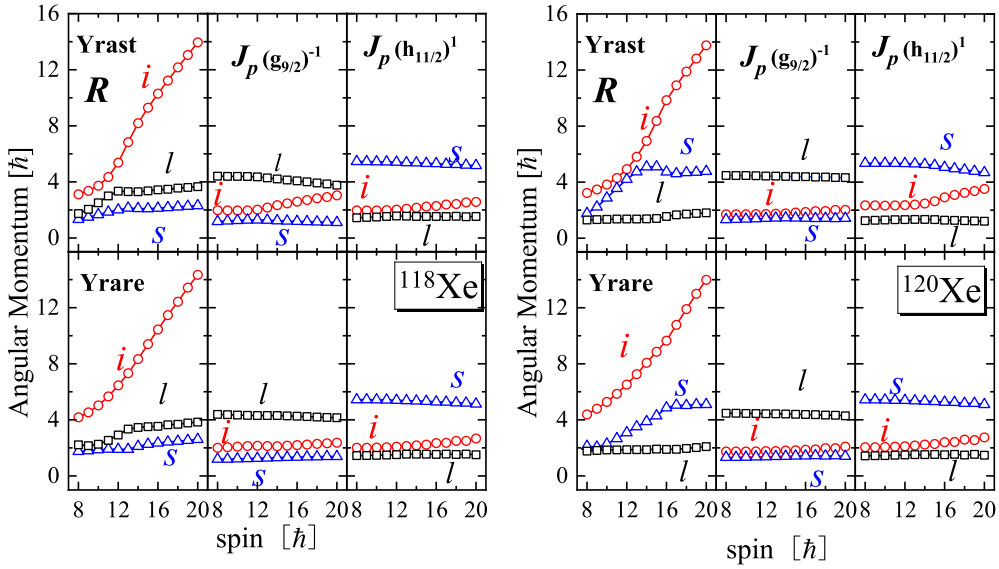


FIG. 4. The root-mean-square components along the intermediate ($i$, circles), short ($s$, triangles), and long ($l$, squares) axes of the core and valence proton angular momenta calculated as functions of spin $I$ by means of the PRM for the yrast and yrare bands with the $\pi g_{9/2}^{-1} \otimes \pi h_{11/2}^{1}$ configuration in $^{118}$Xe (left) and $^{120}$Xe (right). The deformation parameters adopted for $^{118}$Xe and $^{120}$Xe are ($\beta = 0.26$, $\gamma = 34.8^\circ$) and ($\beta = 0.29$, $\gamma = 21.3^\circ$), respectively.

proton $J_p(h_{11/2})^1$ for the yrast and yrare bands with the $\pi g_{9/2}^{-1} \otimes \pi h_{11/2}^{1}$ configuration in $^{118}$Xe and $^{120}$Xe, calculated by PRM. As shown in Fig. 4, the angular momentum of the $g_{9/2}$ valence proton hole and the $h_{11/2}$ valence proton particle in $^{118}$Xe and $^{120}$Xe mainly lie along the long axis ($l$ axis) and the short axis ($s$ axis), respectively. The angular momentum of the collective core $R$ in both isotopes has the largest component along the intermediate axis ($i$ axis). Such orientations establish the chiral geometry of aplanar rotation for the $\pi g_{9/2}^{-1} \otimes \pi h_{11/2}^{1}$ bands in $^{118}$Xe and $^{120}$Xe.

### C. Systematic study

To systematically investigate the physical characteristics of the rotational bands based on the proposed chiral configuration $\pi g_{9/2}^{-1} \otimes \pi h_{11/2}^{1}$, the excitation energies $E(I)$, energy staggering parameters $S(I) = [E(I) - E(I-1)]/2I$, and kinematic moments of inertia $J^{(1)}$ for bands 1 in $^{118}$Xe [15] and $^{120}$Xe [16] were extracted and plotted in Fig. 5. As a comparison, data of the chiral doublet bands based on the $\pi g_{9/2}^{-1} \otimes \nu h_{11/2}^{1}$ configuration in $^{98}$Tc [51], $^{100}$Tc [52], $^{102}$Rh [53], $^{104}$Rh [54], $^{106}$Rh [55], and $^{104}$Ag [56] are also presented. Both asymmetric configurations are composed of one $g_{9/2}$ hole and one $h_{11/2}$ particle, differing primarily in the types of fermions for the valence nucleons. This comparison contributes to exploring the manifestation of chirality in these two systems.

It is well known that the ideal chiral doublet bands exhibit two key characteristics in their energy spectra [57]: (1) the near degeneracy of doublet bands; (2) constant $S(I)$ as a function of spin. As illustrated in Fig. 5, the $\pi g_{9/2}^{-1} \otimes \pi h_{11/2}^{1}$ bands are established at relatively high excitation energies due to the cross-shell excitations. This partially explains the absence of the partner bands and presents a challenge for their population in experiments. In the middle panel, the $S(I)$ curves of the $\pi g_{9/2}^{-1} \otimes \pi h_{11/2}^{1}$ bands are flatter than those of the chiral doublet bands with the $\pi g_{9/2}^{-1} \otimes \nu h_{11/2}^{1}$ configuration, thereby satisfying the second characteristic of chirality in energy spectra. The flatter $S(I)$ curves for the $\pi g_{9/2}^{-1} \otimes \pi h_{11/2}^{1}$ configuration are likely due to the smaller Coriolis interaction, which may partially arise from the ideal particle-hole characteristics of this configuration. These characteristics facilitate a more effective alignment of the particle and hole angular momenta along the $s$ and $l$ axes, respectively, leading to a more orthogonal coupling with the collective angular momentum of the core. In addition, the degree of $\gamma$ softness of the core and the effect of the residual nucleon-nucleon interaction may also contribute to the energy staggering [51,58].

The bottom panel displays the kinematic moments of inertia $J^{(1)} = I/[E(I) - E(I-1)]$ as a function of spin. Reference [13] pointed out that the $I$ independence of $J^{(1)}$ serves as an evidence for an aplanar geometry of the angular momentum. Normally, the $J^{(1)}$ for chiral doublet bands remains nearly constant as spin increases, as demonstrated in $^{98}$Tc, $^{100}$Tc, $^{102}$Rh, $^{104}$Rh, and $^{106}$Rh nuclei (except for $^{104}$Ag). In both $^{118}$Xe and $^{120}$Xe, the behavior of $J^{(1)}$ is highly consistent with the characteristics observed in the aforementioned chiral nuclei. Thus, the systematic study of excitation energies, the staggering parameters, and moments of inertia further support the possibility of chirality in the $\pi g_{9/2}^{-1} \otimes \pi h_{11/2}^{1}$ bands in $^{118}$Xe and $^{120}$Xe.

To further explore the manifestation of chirality under different coupling modes for nucleon types, a systematic analysis of the $B(M1)$ and $B(E2)$ transition probabilities is essential, as they serve as important probes for investigating nuclear intrinsic structure. Currently, no lifetime measurements are

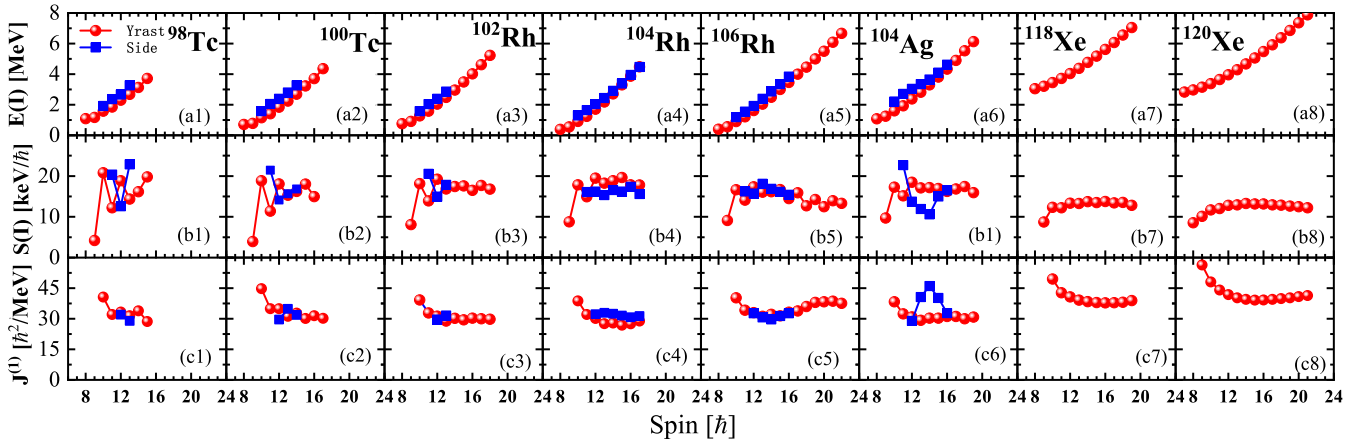


FIG. 5. The excitation energies $E(I)$ (a), the energy staggering parameter $S(I)$ (b), and the kinematic moments of inertia $J^{(1)}$ (c) as a function of spin for the chiral doublet bands with the $\pi g_{9/2}^{-1} \otimes \nu h_{11/2}^{1}$ configuration in $^{98}$Tc [51], $^{100}$Tc [52], $^{102}$Rh [53], $^{104}$Rh [54], $^{106}$Rh [55], $^{104}$Ag [56], as well as the bands 1 with the $\pi g_{9/2}^{-1} \otimes \pi h_{11/2}^{1}$ configuration in $^{118}$Xe [15] and $^{120}$Xe [16].

available for the $\pi g_{9/2}^{-1} \otimes \pi h_{11/2}^{1}$ bands in $^{118}$Xe and $^{120}$Xe. Given the good agreement between our PRM calculations and experimental data for these isotopes (see Sec. II B), the reliability of the present theoretical predictions is well supported. Therefore, the calculated $B(M1)$ and $B(E2)$ values of the doublet bands with the $\pi g_{9/2}^{-1} \otimes \pi h_{11/2}^{1}$ configuration in $^{118}$Xe and $^{120}$Xe from this work are adopted, as shown in Fig. 6. For comparison, the corresponding values of the $\pi g_{9/2}^{-1} \otimes \nu h_{11/2}^{1}$ chiral bands in $^{102,104,106}$Rh are also included in Fig. 6. The values for $^{102}$Rh and $^{104}$Rh are taken from previous experimental measurements [53,59]. For $^{106}$Rh, due to the lack of experimental data, we adopted the PRM calculated results from Ref. [60], which employs the same theoretical framework as our work.

As shown in Fig. 6, for the yrast and yrare bands with the $\pi g_{9/2}^{-1} \otimes \pi h_{11/2}^{1}$ configuration in $^{118,120}$Xe, both intraband $B(M1)$ and $B(E2)$ values are nearly identical. In these nuclei, the intraband $B(E2)$ values are much larger than the interband ones (except the lower spin region in $^{118}$Xe), and the interband $E2$ transitions vanish at higher spins. These characteristics are similar to those calculated for the $\pi g_{9/2}^{-1} \otimes \nu h_{11/2}^{1}$ configuration in $^{106}$Rh and consistent with the suggested ideal chiral criteria [57]. However, compared to the $\pi g_{9/2}^{-1} \otimes \nu h_{11/2}^{1}$ configuration in Rh, the $B(M1)$ values for the $\pi g_{9/2}^{-1} \otimes \pi h_{11/2}^{1}$ configuration in Xe exhibit some unique features: (1) The $B(M1)$ values in Xe isotopes (maximum $\sim 1\mu_N^2$) are significantly smaller than those in Rh isotopes. Such small $B(M1)$ values are also predicted in the chiral doublet bands based

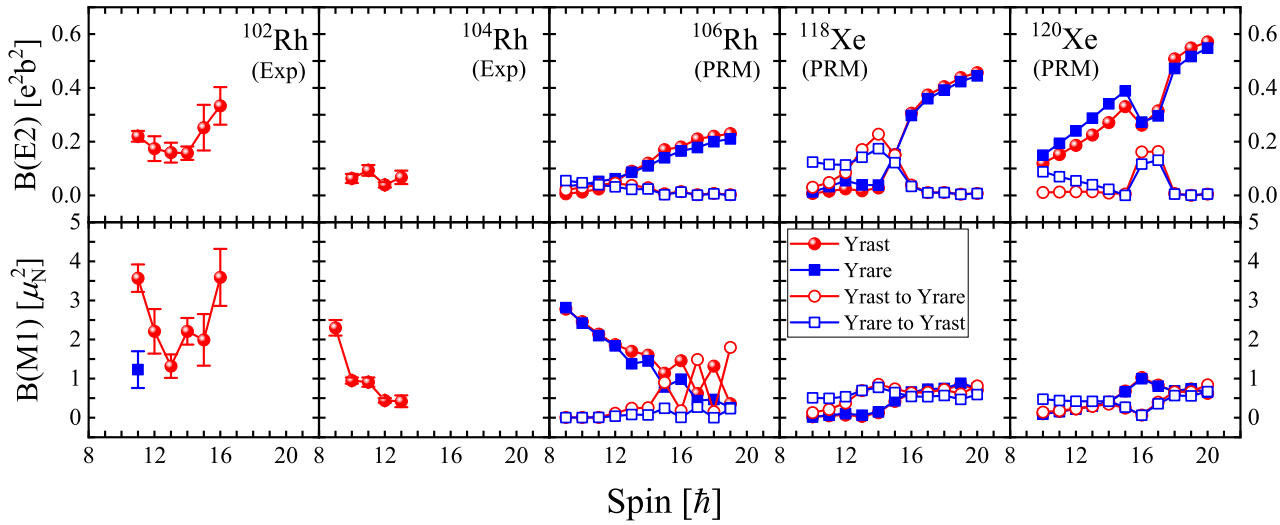


FIG. 6. Comparison of the $B(E2)$ and $B(M1)$ transition probabilities as a function of spin for the $\pi g_{9/2}^{-1} \otimes \nu h_{11/2}^{1}$ bands in $^{102,104,106}$Rh, and the $\pi g_{9/2}^{-1} \otimes \pi h_{11/2}^{1}$ bands in $^{118,120}$Xe. The $B(M1)$ and $B(E2)$ values for $^{102}$Rh and $^{104}$Rh are taken from the experimental measurements [53,59], while those for $^{106}$Rh are derived from PRM calculations in Ref. [60], with deformation parameters $\beta = 0.251$, $\gamma = 23.1^\circ$. The $B(M1)$ and $B(E2)$ values for $^{118}$Xe and $^{120}$Xe are adopted from the PRM calculation in the present work. Solid circles, solid squares, open circles, and open squares represent the intraband transitions of the yrast band, the intraband transitions of the yrare band, the interband transitions from the yrast band to the yrare band, and the interband transitions from the yrare band to yrast band, respectively.

on the neutron-neutron coupling [61]. This phenomenon can be partially attributed to the differences in coupling modes of configurations. (2) In the lower spin region, the intraband $B(M1)$ values in Xe and Rh isotopes display opposite trends with increasing spin. Specifically, Rh isotopes show a gradual decrease, while Xe isotopes demonstrate a slight overall increasing trend. (3) In the higher spin region, the $B(M1)$ values of $^{102}$Rh and $^{106}$Rh display a noticeable odd-even spin staggering, while such behavior is absent in $^{118}$Xe and $^{120}$Xe, possibly related to differences in the $\gamma$ values.

## IV. SUMMARY

In this study, we systematically investigated the existence of chirality in the coupling of the same kind of fermions using the adiabatic and configuration-fixed constrained triaxial CDFT. The $\pi g_{9/2}^{-1} \otimes \pi h_{11/2}^{1}$ configuration in Xe isotopes is based on such a coupling and involves high-$j$ particle-hole characteristics, providing a good case for this investigation. The CDFT calculated results show that the $\pi g_{9/2}^{-1} \otimes \pi h_{11/2}^{1}$ configurations in $^{116\text{–}126}$Xe exhibit significant triaxial deformations favorable for chirality. Based on these results, we propose a new type of chiral system formed by the coupling of valence protons. At the same time, the even-even Xe isotopes naturally become promising candidates for chiral nuclei.

Moreover, the rotational bands based on the $\pi g_{9/2}^{-1} \otimes \pi h_{11/2}^{1}$ configuration have already been reported in $^{118}$Xe and $^{120}$Xe. Using the deformation parameters obtained from CDFT, we further analyzed these bands with the PRM model. The energy spectra and $B(M1)/B(E2)$ ratios calculated by PRM are in good agreement with experimental data, validating the CDFT predictions. To gain a deeper understanding of the manifestation of chirality in this configuration, we performed a systematic study of the excitation energies $E(I)$, energy staggering parameters $S(I)$, and kinematic moments of inertia $J^{(1)}$ for the $\pi g_{9/2}^{-1} \otimes \pi h_{11/2}^{1}$ bands in $^{118}$Xe and $^{120}$Xe. The results show that the characteristics in energy spectra of these bands are consistent with ideal chiral bands. The combination of the PRM calculations and systematic study further supports the existence of chirality in the $\pi g_{9/2}^{-1} \otimes \pi h_{11/2}^{1}$ configuration. Finally, a detailed analysis of the $B(E2)$ and $B(M1)$ values, calculated by PRM in this work, was performed for the candidate chiral bands with the $\pi g_{9/2}^{-1} \otimes \pi h_{11/2}^{1}$ configuration in $^{118}$Xe and $^{120}$Xe. These values were then compared with those of the $\pi g_{9/2}^{-1} \otimes \nu h_{11/2}^{1}$ chiral bands in $^{102}$Rh, $^{104}$Rh, and $^{106}$Rh. It is found that the $B(M1)$ values for the two-proton configuration exhibit unique characteristics in both magnitude and behavior.

This study would not only expands the research scope of chiral configurations but also contributes to exploring the key scientific question regarding the universality of nuclear chirality. Further experimental efforts to search for the partner of the $\pi g_{9/2}^{-1} \otimes \pi h_{11/2}^{1}$ band in $^{118}$Xe and $^{120}$Xe are necessary to verify the existence of chirality. In this regard, this work sheds light on the manifestation of chirality in proton-proton coupling system and provides some references for subsequent experimental studies.

## ACKNOWLEDGMENTS

We thank Prof. S. Y. Wang for detailed guidance. This work is partly supported by the National Natural Science Foundation of China (Grants No. 12105154, No. 12405138, No. 12475123), the Shandong Natural Science Foundation (Grants No. ZR2020QA084), Hubei Provincial Natural Science Foundation of China (Grant No. 2023AFB035), Natural Science Research Project of Yichang City (Grant No. A23-2-028), and the Young Teachers' Development Fund of Harbin Institute of Technology, Weihai (Grant No. IDGA10002235).

## DATA AVAILABILITY

No data were created or analyzed in this study.

[1] S. Frauendorf and J. Meng, Nucl. Phys. A **617**, 131 (1997).
[2] K. Starosta, T. Koike, C. J. Chiara *et al.*, Phys. Rev. Lett. **86**, 971 (2001).
[3] B. A. Bark, E. O. Lieder, R. M. Lieder *et al.*, Int. J. Mod. Phys. E **23**, 1461001 (2014).
[4] S. Frauendorf, Rev. Mod. Phys. **73**, 463 (2001).
[5] J. Meng, B. Qi, S. Q. Zhang *et al.*, Mod. Phys. Lett. A **23**, 2560 (2008).
[6] J. Meng and S. Q. Zhang, J. Phys. G **37**, 064025 (2010).
[7] K. Starosta and T. Koike, Phys. Scr. **92**, 093002 (2017).
[8] S. Frauendorf, Phys. Scr. **93**, 043003 (2018).
[9] B. W. Xiong and Y. Y. Wang, At. Data Nucl. Data Tables **125**, 193 (2019).
[10] S. Y. Wang, Chin. Phys. C **44**, 112001 (2020).
[11] S. Y. Wang, C. Liu, B. Qi *et al.*, Front. Phys. **18**, 64601 (2023).
[12] B. M. Musangu, E. H. Wang, J. H. Hamilton *et al.*, Phys. Rev. C **104**, 064318 (2021).
[13] S. J. Zhu, J. H. Hamilton, A. V. Ramayya *et al.*, Eur. Phys. J. A **25**, 459 (2005).
[14] Y. X. Luo, S. J. Zhu, J. H. Hamilton *et al.*, Phys. Lett. B **670**, 307 (2009).
[15] J. M. Sears, D. B. Fossan, G. R. Gluckman, J. F. Smith, I. Thorslund, E. S. Paul, I. M. Hibbert, and R. Wadsworth, Phys. Rev. C **57**, 2991 (1998).
[16] S. Törmänen, S. Juutinen, R. Julin *et al.*, Nucl. Phys. A **572**, 417 (1994).
[17] J. Hattula, S. Juutinen, M. Jääskeläinen *et al.*, J. Phys. G: Nucl. Phys. **13**, 57 (1987).
[18] A. Al-Khatib, H. Hübel, P. Bringel *et al.*, Eur. Phys. J. A **36**, 21 (2008).
[19] C. M. Petrache, B. F. Lv, A. Astier *et al.*, Phys. Rev. C **97**, 041304(R) (2018).
[20] C. M. Petrache, S. Frauendorf, M. Matsuzaki *et al.*, Phys. Rev. C **86**, 044321 (2012).
[21] J. Meng, J. Peng, S. Q. Zhang, and S.-G. Zhou, Phys. Rev. C **73**, 037303 (2006).
[22] J. M. Yao, B. Qi, S. Q. Zhang, J. Peng, S. Y. Wang, and J. Meng, Phys. Rev. C **79**, 067302 (2009).

[23] S. Y. Wang, B. Qi, L. Lei *et al.*, Phys. Lett. B **703**, 40 (2011).
[24] B. Qi, H. Jia, N. B. Zhang, C. Liu, and S. Y. Wang, Phys. Rev. C **88**, 027302 (2013).
[25] I. Kuti, Q. B. Chen, J. Timár *et al.*, Phys. Rev. Lett. **113**, 032501 (2014).
[26] C. Liu, S. Y. Wang, R. A. Bark *et al.*, Phys. Rev. Lett. **116**, 112501 (2016).
[27] E. Grodner, J. Srebrny, Ch. Droste *et al.*, Phys. Rev. Lett. **120**, 022502 (2018).
[28] B. Qi, H. Jia, C. Liu, and S. Y. Wang, Phys. Rev. C **98**, 014305 (2018).
[29] J. Li, Phys. Rev. C **97**, 034306 (2018).
[30] J. Peng and Q. B. Chen, Phys. Lett. B **806**, 135489 (2020).
[31] W. Z. Xu, S. Y. Wang, X. G. Wu *et al.*, Phys. Lett. B **839**, 137789 (2023).
[32] A. D. Ayangeakaa, U. Garg, M. D. Anthony *et al.*, Phys. Rev. Lett. **110**, 172504 (2013).
[33] H. Jia, S. Y. Wang, B. Qi *et al.*, Phys. Lett. B **833**, 137303 (2022).
[34] R. J. Guo, S. Y. Wang, C. Liu *et al.*, Phys. Rev. Lett. **132**, 092501 (2024).
[35] Q. B. Chen, N. Kaiser, UIf-G. Meißner *et al.*, Phys. Lett. B **807**, 135568 (2020).
[36] Q. B. Chen, B. F. Lv, C. M. Petrache *et al.*, Phys. Lett. B **782**, 744 (2018).
[37] J. Peng, J. Meng, and S. Q. Zhang, Phys. Rev. C **68**, 044324 (2003).
[38] B. Qi, S. Q. Zhang, S. Y. Wang, J. M. Yao, and J. Meng, Phys. Rev. C **79**, 041302(R) (2009).
[39] J. Peng, H. Sagawa, S. Q. Zhang, J. M. Yao, Y. Zhang, and J. Meng, Phys. Rev. C **77**, 024309 (2008).
[40] J. M. Yao, H. Chen, and J. Meng, Phys. Rev. C **74**, 024307 (2006).
[41] J. Li, Y. Zhang, J. M. Yao, and J. Meng, Sci. China Ser. G **52**, 1586 (2009).
[42] Q. B. Chen, J. M. Yao, S. Q. Zhang, and B. Qi, Phys. Rev. C **82**, 067302 (2010).
[43] H. Jia, B. Qi, S. Y. Wang *et al.*, Chin. Phys. C **40**, 124103 (2016).
[44] P. W. Zhao, Z. P. Li, J. M. Yao, and J. Meng, Phys. Rev. C **82**, 054319 (2010).
[45] G. D. Dracoulis, G. J. Lane, A. P. Byrne *et al.*, Phys. Lett. B **709**, 59 (2012).
[46] M. W. Reed, G. J. Lane, G. D. Dracoulis *et al.*, Phys. Lett. B **752**, 311 (2016).
[47] T. Shizuma, P. D. Stevenson, P. M. Walker, Y. Toh, T. Hayakawa, M. Oshima, K. Furuno, and T. Komatsubara, Phys. Rev. C **65**, 064310 (2002).
[48] X. Xiao, S. Y. Wang, C. Liu *et al.*, Phys. Rev. C **106**, 064302 (2022).
[49] W. Z. Xu, D. P. Sun, S. Y. Wang *et al.*, Phys. Rev. C **109**, 044303 (2024).
[50] J. Peng and Q. B. Chen, Phys. Lett. B **793**, 303 (2019).
[51] Ding Huai-Bo, S. J. Zhu, J. G. Wang *et al.*, Chin. Phys. Lett. **27**, 072501 (2010).
[52] P. Joshi, A. R. Wilkinson, T. Koike *et al.*, Eur. Phys. J. A **24**, 23 (2005).
[53] D. Tonev, M. S. Yavahchova, N. Goutev *et al.*, Phys. Rev. Lett. **112**, 052501 (2014).
[54] C. Vaman, D. B. Fossan, T. Koike, K. Starosta, I. Y. Lee, and A. O. Macchiavelli, Phys. Rev. Lett. **92**, 032501 (2004).
[55] P. Joshi, D. G. Jenkins, P. M. Raddon *et al.*, Phys. Lett. B **595**, 135 (2004).
[56] Z. G. Wang, M. L. Liu, Y. H. Zhang *et al.*, Phys. Rev. C **88**, 024306 (2013).
[57] S. Y. Wang, S. Q. Zhang, B. Qi *et al.*, Chin. Phys. Lett. **24**, 664 (2007).
[58] E. A. Lawrie, P. A. Vymers, J. J. Lawrie *et al.*, Phys. Rev. C **78**, 021305(R) (2008).
[59] T. Suzuki, G. Rainovski, T. Koike *et al.*, Phys. Rev. C **78**, 031302(R) (2008).
[60] S. Y. Wang, S. Q. Zhang, B. Qi, J. Peng, J. M. Yao, and J. Meng, Phys. Rev. C **77**, 034314 (2008).
[61] B. Qi, S. Y. Wang, and S. Q. Zhang, Chin. Phys. Lett. **28**, 122101 (2011).